

Impact of signal non-repeatability on spectral CT images

Gilad Shechter¹

Abstract– We formulate the dependency of band/ring artifacts in spectral CT images on the detector signal non-repeatability. For this purpose we introduce functionals that are proportional to the level of artifacts and contain variables that are measured in the signal domain by non-rotating scans. We set thresholds for these functionals by simulations of rotating scans and use these thresholds to analyze the level of artifacts in a realistic spectral CT system.

I. INTRODUCTION

Projection domain decomposition [1] is used widely today in spectral CT systems based on different strategies like kVp switching [2], dual-layer detector [3], and photon counting detector [4]. The decomposed line integrals in these systems are reconstructed to create basis spectral images such as photo/scatter, water/iodine, or to create a three element image basis for K-edge imaging. Spectral results of clinical relevance, e.g. virtual mono-energetic (monoE) images are then derived from the basis images. We study the creation of band/ring artifacts as a result of detector signal non-repeatability in monoE and conventional single-energy images.

II. METHODS

A. Methodology

Performing a measurement of the non-repeatability of each individual detector pixel with a satisfying signal-to-noise ratio (SNR) might be too time consuming. Furthermore, it is not fully clear how to associate the signal non-repeatability of individual pixels with the net level of image artifacts. Due to these reasons we model the detector signal non-repeatability as having two components – an average component and a fluctuating component with respect to the pixels belonging to the same detector module. For each of these two components we introduce below a suitable functional that expresses the contribution of that component to the distortion of the decomposed line integrals. The values of these functionals measured from non-rotating scans allow us to estimate the level of band/ring artifacts in image reconstructed from rotating scans.

Average component

Let $s_d^v(S)$ denote the signal of detector pixel d measured at energy bin v , and averaged over all integration periods (IP) of the scan S . For the Philips dual layer IQon scanner, the index

$v \in \{l, h\}$ stands for the layer in which the signal is collected. For a photon counting system, this index refers here to a two-sided energy bin, i.e. to photons detected between two energy thresholds. The variation of $s_d^v(S)$ from one scan to another may stem from A. Poisson noise. B. Signal non-repeatability. In (1), $\hat{s}_d^v(S_1, S_2)$ is defined as the relative signal difference between the scans S_1 and S_2 . Let $p_{be}^d(S)$ denote the decomposed line integrals of the de-composition basis element be (e.g. photo/scatter) obtained by averaging the readings of pixel d over all IP of a non-rotating scan. Let $p_{be}^m(S)$ be the average of $p_{be}^d(S)$ across the detector pixels of module m . Finally, let M be the number of detector pixels per module. Using these notations, we have (2).

(1)

$$\Delta \hat{s}_d^v(S_1, S_2) \equiv \frac{s_d^v(S_2) - s_d^v(S_1)}{s_d^v} ; s_d^v \equiv \frac{s_d^v(S_1) + s_d^v(S_2)}{2}.$$

(2)

$$\begin{aligned} \Delta p_{be}^m(S_1, S_2) &\equiv \frac{1}{M} \sum_{d \in m} \Delta p_{be}^d(S_1, S_2) \approx \\ &\frac{1}{M} \cdot \sum_{d \in m} \sum_v s_d^v \cdot \frac{\partial p_{be}^d}{\partial s_d^v} \Big|_{s_d^v} \cdot \Delta \hat{s}_d^v(S_1, S_2) \approx \\ &\sum_v H_{be}^v \cdot \Delta \hat{s}_{ave}^v(m, S_1, S_2) \equiv \Delta A_{be}(m, S_1, S_2) ; \\ H_{be}^v(m) &\equiv \frac{1}{M} \cdot \sum_{d \in m} s_d^v \cdot \frac{\partial p_{be}^d}{\partial s_d^v} \Big|_{s_d^v} ; \\ \Delta \hat{s}_{ave}^v(m, S_1, S_2) &\equiv \frac{1}{M} \cdot \sum_{d \in m} \Delta \hat{s}_d^v(S_1, S_2) ; \\ \Delta p_{be}^d(S_1, S_2) &\equiv p_{be}^d(S_2) - p_{be}^d(S_1). \end{aligned}$$

The term $H_{be}^v(m)$ in (2) depends of course on the object that is intersected by the ray paths. The variables $\Delta \hat{s}_{ave}^v$ represent the signal non-repeatability averaged not only over the plurality of projections but also over different detector pixels within the module. Therefore, they can be measured with only a negligible impact of the Poisson noise. Consider now a scenario in which the two non-rotating scans S_1 and S_2 performed at times t_1 and $t_2 > t_1$ respectively had been replaced by a calibration scan performed in t_1 and a successive object scan performed at t_2 .

¹ Philips medical technologies LTD., Haifa, Israel

From CT reconstruction principles, as well as due to the equality derived in (2), the level of module-dependent bands that would be obtained in the image reconstructed from these calibration and object scans is proportional to the variation of $\Delta A_{be}(m, S_1, S_2)$ along the modules. Note that these functionals vary for different spectrally decomposed basis elements.

Fluctuating component

Next, we consider the signal non-repeatability component that fluctuates across the detector module pixels. This component leads as defined in (3) to a fluctuating non-repeatability of the de-composed line integrals associated with the spectral basis element be . Note that by definition $\text{var}_{be}^m(S_1, S_2)$ in (3) is containing only the variations induced by signal non-repeatability excluding the contribution of the Poisson noise distribution of the photon probability not to be attenuated within the scanned object. A similar derivation to that done in (2) connects between $\text{var}_{be}^m(S_1, S_2)$ and between measured signal non-repeatability variables, see (4).

(3)

$$\text{var}_{be}^m(S_1, S_2) \equiv \frac{1}{M} \cdot \sum_{d \in m} (\Delta p_{be}^d(S_1, S_2) - \Delta p_{be}^m(S_1, S_2))^2.$$

(4)

$$\begin{aligned} \text{var}_{be}^m(S_1, S_2) &\approx \sum_{vv'} G_{be}^{vv'} \cdot C^{vv'} \equiv \Delta F_{be}(m, S_1, S_2); \\ G_{be}^{vv'}(m) &\equiv \frac{1}{M} \cdot \sum_{d \in m} s_d^v \cdot s_d^{v'} \cdot \frac{\partial p_{be}}{\partial s_d^v} \Big|_{s_d^{v'}} \cdot \frac{\partial p_{be}}{\partial s_d^{v'}} \Big|_{s_d^{v'}}; \\ C^{vv'}(m) &\equiv \frac{1}{M} \cdot \sum_{d \in m} \Delta \hat{s}_d^v(S_1, S_2) \cdot \Delta \hat{s}_d^{v'}(S_1, S_2) - \\ &\Delta \hat{s}_{ave}^v(m, S_1, S_2) \cdot \Delta \hat{s}_{ave}^{v'}(m, S_1, S_2) - \\ &\delta_{vv'} \cdot \left[\frac{1}{M} \cdot \sum_{d \in m} \Delta \hat{s}_d^v(S_1, S_2) \cdot \Delta \hat{s}_d^{v'}(S_1, S_2) \right]_p. \end{aligned}$$

The diagonal last term of $C^{vv'}(m)$ stands for the contribution of the Poisson noise, symbolized by $[\]_p$ to the second power of $s_d^v(S)$ averaged across the pixels. Having a polychromatic spectral model for the system allows pre-calculating this term based on the scan parameters. Note that this term like the other terms of $C^{vv'}(m)$ can be calculated with a much better SNR with respect to the individual $\Delta \hat{s}_d^v$. In similarity to the case of an average component discussed above, the level of ring image artifacts that would be present in an image reconstructed based on a calibration scan and an object scan performed at t_1 and t_2 respectively should be proportional to the square root of $\text{var}_{be}^m(S_1, S_2)$. Following (4), this level of

ring artifacts should be also proportional to the square root of $\Delta F_{be}(m, S_1, S_2)$.

B. Validation by simulations

To confirm our last expectation, we simulated three noiseless circular scans of a 150 mm diameter water phantom concentric with the rotation center. We assumed a system of 3 energy bins with a spectral behavior uniform for all detector modules, see Fig. 1. For this spectral behavior we calculated numerically the matrices $G_{be}^{vv'}$ assuming each ray is attenuated by 150 mm of water. The values of $C^{vv'}$ selected for the three simulations are given by (5). Random values of $\Delta \hat{s}_d^v$ for the individual pixels that are forced to be in agreement with these selected values of $C^{vv'}$ were obtained by a standard Cholesky [5] decomposition. From the simulated scans described above we decomposed and reconstructed a water image and a pair of photo/scatter images. Fig. 2 confirms the linear dependence of the level of ring artifacts on the square root of $\Delta F_{w,p,s}$. Here, the subscripts w , p and s stand for the water, photo and scatter images respectively. The ring level denoted by R_l was taken as the absolute value of the rings averaged within a 130 mm diameter circular field of view.

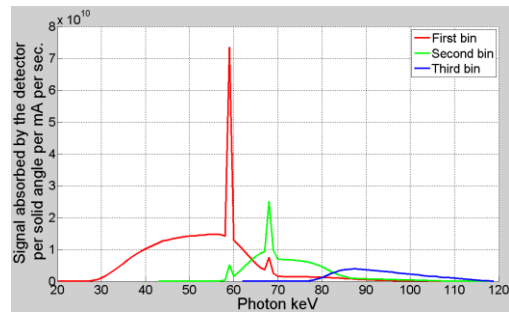


Figure 1. Signal spectral behavior for air scan, including tube flux and detector response for a 3-energy bin scanner.

(5)

$$\begin{aligned} C_{sim.1}^{vv'} &= 8 \cdot \delta_{v,1} \cdot \delta_{v,1} + 2 \cdot \delta_{v,2} \cdot \delta_{v,2} - 0.5 \cdot (\delta_{v,1} \cdot \delta_{v,2} + \delta_{v,2} \cdot \delta_{v,1}) \\ C_{sim.2}^{vv'} &= 8 \cdot \delta_{v,2} \cdot \delta_{v,2} + 2 \cdot \delta_{v,3} \cdot \delta_{v,3} - 0.5 \cdot (\delta_{v,2} \cdot \delta_{v,3} + \delta_{v,3} \cdot \delta_{v,2}) \\ C_{sim.3}^{vv'} &= 6 \cdot \delta_{v,3} \cdot \delta_{v,3} + 4 \cdot \delta_{v,1} \cdot \delta_{v,1} + 2 \cdot (\delta_{v,1} \cdot \delta_{v,3} + \delta_{v,3} \cdot \delta_{v,1}). \end{aligned}$$

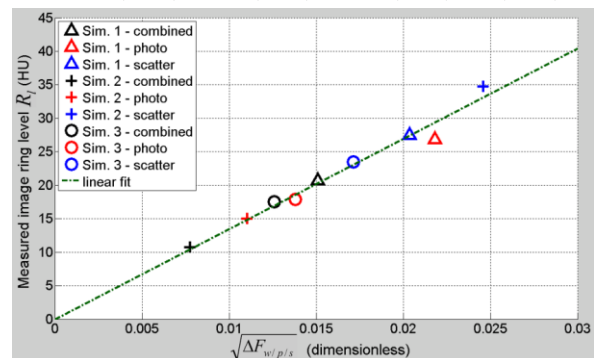


Figure 2. Dependency of the measured ring level on the predicted one.

C. Determining tolerance thresholds

In this section we address by example the tolerance of the functionals associated with the level of bands. Finding this tolerance using $\Delta A_{p/s}(m)$ i.e. the photo/scatter material decomposition basis is somewhat ambiguous: because of the slight difference between the energy dependence of these mechanisms in different materials, because of the option to add the Rayleigh scatter mechanism to the photo mechanism (due to their similarity in energy dependence), and due to the arbitrary scaling of the photo/scatter images. In contrast, monoE images obtained as linear combinations of the photo/scatter images, are well defined and contain an objective clinical meaning. We therefore look for tolerance thresholds in the signal domain corresponding to a tolerable level of bands in 40-keV, 70-keV and 120-keV monoE images. For this purpose, we define the keV-dependent functionals associated with the level of bands in monoE images in (6). Here, the coefficients $\alpha_{p/s}$ are those used to generate the monoE image as a linear combination of the photo and scatter images reconstructed from the decomposed photo/scatter line integrals. Due to the linearity of the reconstruction, we can write those functionals as in (7).

(6)

$$\Delta A_{keV}^{mono}(m) = \alpha_p(keV) \cdot \Delta A_p(m) + \alpha_s(keV) \cdot \Delta A_s(m).$$

(7)

$$\Delta A_{keV}^{mono}(m) = \sum_v H_{keV}^v(m) \cdot \Delta \hat{s}_{ave}^v(m);$$

$$H_{keV}^v(m) \equiv \alpha_p \cdot H_p^v(m) + \alpha_s \cdot H_s^v(m).$$

To find tolerances for the variation of $\Delta A_{keV}^{mono}(m)$ between adjacent modules, we simulated noisy circular scans with the same spectral behavior as in Fig. 1 and the same circular phantom used before. We used 400 mA and 1.0 sec rotation time. We also applied non-linear de-noising algorithms to the reconstructed images [6-7]. We simulated a signal non-repeatability with a relative signal change that alternates together for all energy bins across half of the detector arc, see Fig. 3. In Fig. 4, the images on the upper row were obtained by using the signal non-repeatability described by table 1. Here, the band artifacts are very weak and are partially concealed by the residual low-frequency noise left after image de-noising. For reference, we show on the lower row the images obtained after multiplying the values of $\Delta \hat{s}_{ave}^v(m)$ given in table 1 by a factor of 2. Taking into account the narrow window, thick reconstructed slice width and smooth convolution filter indicated in the caption of Fig. 4, we define tolerance thresholds for the variation of $\Delta A_{keV}^{mono}(m)$ between adjacent modules as the values of these variation corresponding to the images on the upper row and to the relative signal change given in table 1. We

calculated numerically the variables H_{keV}^v for the spectral model shown in Fig. 1 assuming by an approximation 150 mm of water path intersected by all rays. The result of this calculation is shown in table 2, where we also give corresponding values found for the Philips IQon scanner. Substituting this result in (7) together with the amplitudes of $\Delta \hat{s}_{ave}^v(m)$ given by table 1, we end up with the thresholds for the allowed peak to peak variation in $\Delta A_{keV}^{mono}(m)$ between adjacent modules, given in table 3 for the 3- energy bin scanner. The reason for the tighter threshold at 70 keV stems from the lower residual low frequency noise at this keV. In table 3 we also give the corresponding threshold values found for the Philips IQon system based on its own H_{keV}^{mono} see table 2, simulations of the same circular phantom at the same mA and 120 kVp, and reconstructions with the same reconstructed slice width and convolution filter used for the 3-bin system.

keV	v=1	v=2	v=3
40	$4 \cdot 10^{-4}$	0	$4 \cdot 10^{-4}$
70	$3.5 \cdot 10^{-4}$	$3.5 \cdot 10^{-4}$	$3.5 \cdot 10^{-4}$
120	0	$6.0 \cdot 10^{-4}$	0

Table 1. Peak-to-peak variations in $\Delta \hat{s}_{ave}^v(m)$ corresponding to the tolerance threshold at different keV.

keV	3- energy bin scanner			Philips IQon	
	v=1	v=2	v=3	Low-energy bin	High-energy bin
40	-2.10	0.62	0.80	-3.86	2.88
70	-0.19	-0.47	-0.36	-0.19	-0.80
120	0.39	-0.80	-0.71	0.91	-1.91

Table 2. Calculated H_{keV}^{mono} for the 3-bin spectral model, and for the Philips IQon assuming an attenuation through a water path of 150 mm.

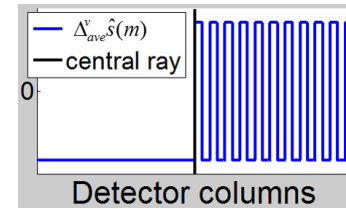


Figure 3. Simulated pattern of the relative signal change $\Delta \hat{s}_{ave}^v(m)$.

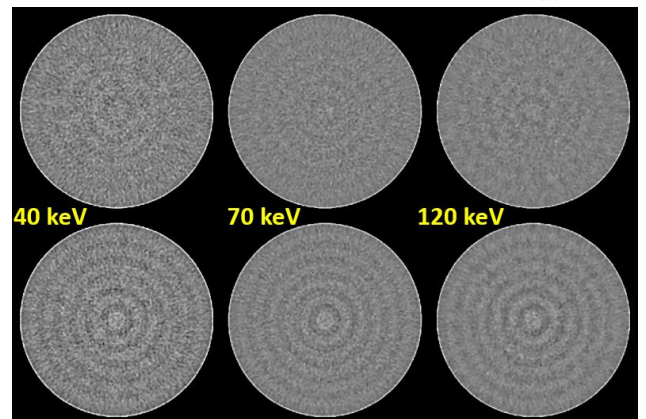


Figure 4. MonoE images for the 3-energy bin scanner. WW (WL)= 40 (0) HU. Reconstructed slice width is 5.0 mm. Filter role off from 2 to 13 1/cm.

keV	$abs(\Delta A_{keV}^{mono}(m+1) - \Delta A_{keV}^{mono}(m))$	
	3- energy bin scanner	Philips IQon
40	$5.2 \cdot 10^{-4}$	$7.2 \cdot 10^{-4}$
70	$3.6 \cdot 10^{-4}$	$3.4 \cdot 10^{-4}$
120	$4.8 \cdot 10^{-4}$	$5.7 \cdot 10^{-4}$

Table 3. Tolerance thresholds for the allowed peak to peak variation between adjacent modules of the signal domain functionals $\Delta A_{keV}^{mono}(m)$.

Realistic spectral CT system

Comparing the values $\Delta A_{keV}^{mono}(m)$ of a real system with the thresholds set for it in table 3, helped us to evaluate the signal non-repeatability of the Philips IQon dual-layer system. We performed two identical non-rotating scans at 120 kVp, with a time gap of three days in between. A Delrin plate of 100 mm length was used as the attenuating object. The values $\Delta \hat{s}_{ave}^{v=l,h}$ measured from these scans for the modules blocked by the Delrin plate are given in Fig. 5. In addition we show in this figure the relative change in the conventional single energy signal $\Delta \hat{s}_{ave}^c$. Substituting the data points in Fig. 5 and the IQon values for H_{keV}^{mono} given in table 2 in (7), we end up with the values of ΔA_{keV}^{mono} captured in Fig. 6.a together with their conventional image counterparts denoted by ΔA_c . The variations of $\Delta A_{keV=40,120}^{mono}$ across the modules are anti-correlated and are larger than those for $\Delta A_{keV=70}^{mono}$ and ΔA_c . This reflects the anti-correlated behavior of ΔA in the photo and scatter images. The tolerance thresholds of ΔA_{keV}^{mono} given in table 3 give the maximal allowed peak to peak variations between adjacent modules belonging to the central part of the detector arc. However, it is well known that the level of band artifacts in reconstructed CT images is proportional not only to the distortion of line integrals expressed in our case by ΔA_{keV}^{mono} but also to the inverse square root of the distance of the band from the rotation center. For this reason, the gaps between the semi-continuous lines representing the tolerance thresholds, are broadened off-center. In Fig. 6.b we compare $\Delta A_{keV=120,140}^{mono}$ to the values obtained for these functionals after replacing $\Delta \hat{s}_{ave}^{v=l,h}$ used in (7) by $\Delta \hat{s}_{ave}^c$. It is clear that $\Delta A_{keV=40,120}^{mono}$ are mostly sensitive to the difference between $\Delta \hat{s}_{ave}^l$ and $\Delta \hat{s}_{ave}^h$.

III. CONCLUSIONS

Avoiding band artifacts induced by signal non-repeatability is more challenging for spectral images than for the conventional image. This is due to the different behavior of the non-repeatability that may arise at different energy bins. Philips's dual detector layer IQon scanner meets this challenge.

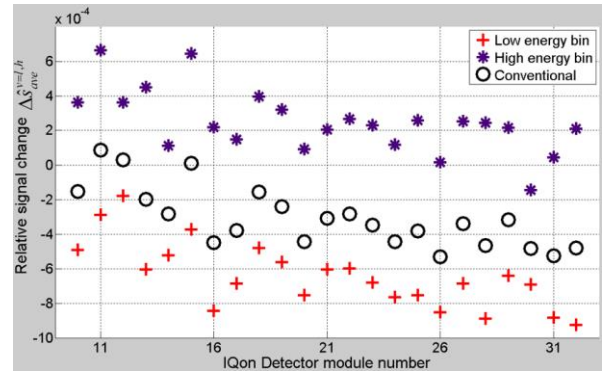


Figure 5. Relative changes of the IQon signals over 3 days for the modules blocked by the Delrin plate.

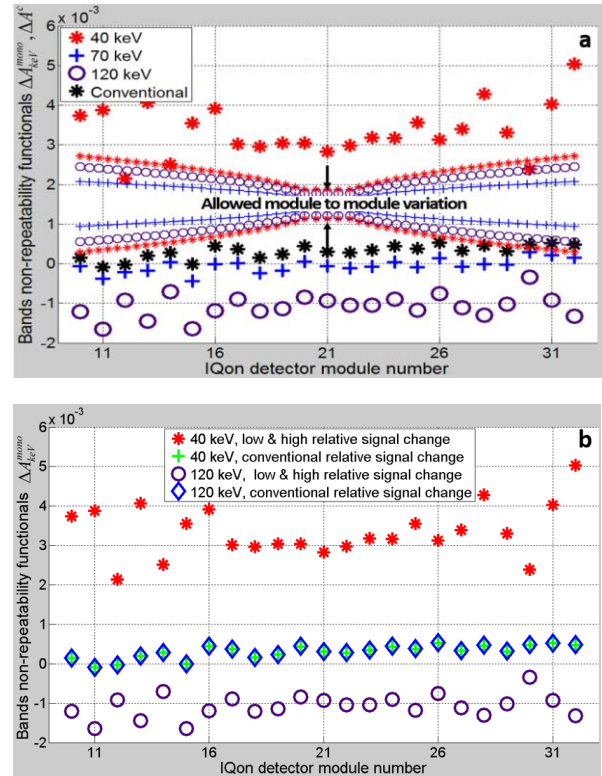


Figure 6. Calculated bands non-repeatability functionals for IQon. In (a) the module to module variations fall within the tolerance thresholds. In (b), these variations fall down further after replacing $\Delta \hat{s}_{ave}^{v=l,h}$ by $\Delta \hat{s}_{ave}^c$.

REFERENCES

- [1] "Energy-selective reconstructions in X-ray computerized tomography", R. E. Alvarez and A. Macovski, Phys. Med. Biol., **21** (1976), p. 733-744.
- [2] "Monochromatic CT image representation via fast switching dual kVp", X. Wu, Proc. SPIE Medical Imaging, **7258** (2009).
- [3] "A dual-energy CT based on a double layer detector", A. Altman and R. Carmi, AAPM Annual Meeting, 2013.
- [4] "K-edge imaging in x-ray computed tomography using multi-bin photon counting detector", E. Roessl and R. Proksa, Phys. Med. Biol., **52** (2007), p. 4679-4696.
- [5] "Sur la résolution numérique des systèmes d'équations linéaires", A. L. Cholesky, Bulletin de la société des amis de la bibliothèque de l'École polytechnique (SABIX), **39** (2005).
- [6] "Structure propagation restoration for spectral CT", Liran Goshen, US patent 2015379694(A1), 2015.
- [7] "Anti-correlated noise filter", Kevin Brow, Liran Goshen, Asher Gringauz, and Stanislav Zabic, patent WO2016103088 (A1), 2016.